Journal of Biomedical Optics

SPIEDigitalLibrary.org/jbo

Simultaneous optical mapping of transmembrane potential and wall motion in isolated, perfused whole hearts

Elliot B. Bourgeois
Andrew D. Bachtel
Jian Huang
Gregory P. Walcott
Jack M. Rogers

SPIE

Simultaneous optical mapping of transmembrane potential and wall motion in isolated, perfused whole hearts

Elliot B. Bourgeois,[a] Andrew D. Bachtel,[a] Jian Huang,[b] Gregory P. Walcott,[b] and Jack M. Rogers[a]
[a]University of Alabama at Birmingham, Department of Biomedical Engineering, Voker Hall B140, 1670 University Boulevard, Birmingham, Alabama 35294
[b]University of Alabama at Birmingham, Department of Medicine, Voker Hall B140, 1670 University Boulevard, Birmingham, Alabama 35294

Abstract. Optical mapping of cardiac propagation has traditionally been hampered by motion artifact, chiefly due to changes in photodetector-to-tissue registration as the heart moves. We have developed an optical mapping technique to simultaneously record electrical waves and mechanical contraction in isolated hearts. This allows removal of motion artifact from transmembrane potential (V_m) recordings without the use of electromechanical uncoupling agents and allows the interplay of electrical and mechanical events to be studied at the whole organ level. Hearts are stained with the voltage-sensitive dye di-4-ANEPPS and ring-shaped markers are attached to the epicardium. Fluorescence, elicited on alternate frames by 450 and 505 nm light-emitting diodes, is recorded at 700 frames/ per second by a camera fitted with a 605 ± 25 nm emission filter. Marker positions are tracked in software. A signal, consisting of the temporally interlaced 450 and 505 nm fluorescence, is collected from the pixels enclosed by each moving ring. After deinterlacing, the 505 nm signal consists of V_m with motion artifact, while the 450 nm signal is minimally voltage-sensitive and contains primarily artifacts. The ratio of the two signals estimates V_m. Deformation of the tissue enclosed by each set of 3 rings is quantified using homogeneous finite strain. [DOI: 10.1117/1.3630115]

Keywords: electromechanical coupling; cardiac electrophysiology; ratiometry; motion tracking.

Paper 10588RRR received Oct. 29, 2010; revised manuscript received Aug. 4, 2011; accepted for publication Aug. 4, 2011; published online Sep. 19, 2011.

1 Introduction

In this report, we present an optical method to simultaneously record transmembrane potential (V_m) and epicardial wall motion from multiple sites on isolated, perfused whole hearts. This technique has two broad applications: First, it allows multisite optical recording of V_m from beating hearts—typically, such recordings require cardiac motion to be arrested with electromechanical uncoupling agents which can affect electrophysiology. Second, it will provide a new way to study the bidirectional interplay between the heart's electrical and mechanical function.

Cardiac electrical activation has been widely studied for decades, but almost always independently from mechanical contraction. Cardiac propagation can be mapped by affixing electrodes to the muscle (electrical mapping)[1] or by staining the tissue with a voltage-sensitive fluorescent dye and recording cardiac waves with high speed photodetectors (optical mapping).[2] Optical mapping is advantageous relative to electrical mapping because optical signals are proportional to transmembrane potential (V_m) and therefore contain repolarization information, which is key to understanding many arrhythmias. Also, because the signals do not contain electrical stimulation artifacts, optical mapping is well-suited to studies of defibrillation.[2] Depending on the choice of photodetector, optical mapping can have a much higher spatial resolution than electrical mapping. However, optical mapping has the major disadvantage that when the heart contracts, correspondence is lost between photodetector pixels and the tissue they image. To deal with this, most optical mapping studies use an electromechanical uncoupling agent (e.g., butanedione monoxime, cytochalasin-D, blebbistatin) to abolish heart motion.[3,4]

Cardiac deformation, independent of electrical function, has been measured in many ways. Ultrasound is often used clinically to qualitatively assess ventricular function.[5] A more quantitative approach is to measure wall motion in terms of strain, a tensor quantity that relates the positions of tissue points in a deformed state relative to an undeformed state. A number of techniques for measuring strain have been developed. For example: tracking tissue points that have been magnetically tagged with MRI;[6,7] tracking the distance between ultrasonic crystals implanted in the muscle;[8] analyzing speckle patterns in ultrasound images;[9] and in isolated hearts, tracking epicardial titanium dioxide markers with high-speed video cameras.[10]

Electrical and mechanical cardiac functions are bidirectionally coupled: not only do electrical waves trigger contraction, but mechanical stimuli can initiate electrical waves via stretch activated channels.[11] However, despite this interdependence, only a few techniques have been developed to produce combined electromechanical maps of activation. Catheter-based systems can track wall motion and electrical activation simultaneously, but

Address all correspondence to: Jack Rogers, University of Alabama at Birmingham, Biomedical Engineering, 1670 University, Boulevard, Volker Hall, B140 Birmingham, Alabama 35294; Tel: 205-975-2102; Fax: 205-975-4720; E-mail: jmr@crml.uab.edu.

1083-3668/2011/16(9)/096020/11/$25.00 © 2011 SPIE

only at one site at a time.[12] Repositioning the catheter between beats permits multisite electromechanical mapping, but requires a stable, repeating rhythm. Others have built electromechanical maps by recording motion at multiple sites for a series of beats, then mapping electrical activation during a subsequent series of beats with an electrode array.[13,14] These methods also require a stable, repeating heart rhythm. We know of only two studies that combine multisite electrical recordings with simultaneous mechanical measurement. In one, bipolar electrodes were embedded in radio-opaque lead markers, and marker positions were recorded via biplane cine radiography. Twenty-five to 53 markers were sutured to the ventricular epicardium and paced beats were mapped electrically and mechanically at the same time.[15] More recently, Seo et al. used epicardial marker tracking to estimate the deformation of cardiac preparations and correct for motion artifact in optical V_m recordings. They used the method to relate deformation to arrhythmia initiation.[16]

In our method, ring-shaped material markers are attached to the isolated heart, which is stained with voltage sensitive dye (VSD). V_m signals are obtained by recording the fluorescence emitted from within each marker and using a ratiometric technique to minimize motion artifact. Mechanical deformation is quantified by tracking the marker positions through frames of video and computing finite strain tensors for the triangles formed by three adjacent markers.

2 Methods

All animal protocols were approved by the University of Alabama at Birmingham Institutional Animal Care and Use Committee.

2.1 *Optical Mapping Apparatus*

Excitation light was provided by 12 royal blue (450 nm peak emission) and 12 cyan (505 nm peak emission) light-emitting diodes (LEDs) (Luxeon Rebel, Philips Lumileds) soldered to 1 cm square metal core printed circuit boards (LXB-RS10, Quadica Developments). Two excitation light colors were used to implement excitation ratiometry. The illumination pattern of the royal blue light must be approximately the same as the illumination pattern of the cyan light so that moving epicardial markers encounter the same changes in light field for both colors. To achieve this configuration, we trimmed the circuit boards so that pairs of royal blue and cyan LEDs could be positioned as close as possible to each other (∼4 mm, emitter-to-emitter). The LED pairs were mounted on heat sinks and positioned around the camera lens to aim the LED light output at the mapped epicardial region. The excitation light was bandpass filtered at 480 ± 45 nm (Omega Optical) to remove residual red light.

Emitted fluorescence was recorded at 700 frames per second (fps) with a CCD camera (iXon DV860DC-BV, Andor Technologies) set to 86 × 128 pixel resolution and fitted with a video lens (6 mm, f/1.0, Pentax) and a 605 ± 25 nm optical bandpass filter (Omega Optical). This configuration produced a spatial resolution of ∼0.4 mm per pixel at typical working distances. Excitation light was alternated between royal blue and cyan with every camera frame. This was done by feeding a 700 Hz digital pulse train generated by the camera into a multichannel pulse generator (Pulsemaster A300, World Precision Instruments) that produced two opposite phase 350 Hz digital signals. These signals controlled the on/off state of custom-made current-regulated LED driver circuits (one bank of driver circuits per excitation light color). To allow time for LED current rise and fall, the square wave driving light alternation was 40 μs shorter than the single camera frame acquisition interval. The on-intensity of excitation light was set by two independent analog controls. Figure 1 shows reflected excitation light recorded by the camera while cyan on-intensity was set to 0 and blue on-intensity was first turned up and then back to 0. Blue-illuminated frames are plotted with gray circles and the alternating cyan frames are plotted with black dots. No excitation light is present during cyan frames, even when blue on-intensity is nonzero, demonstrating that LEDs switch in synchrony with the camera and do not bleed light into adjacent frames. Data from the opposite case (blue off, cyan turned up, and then back to 0) were similar (not shown).

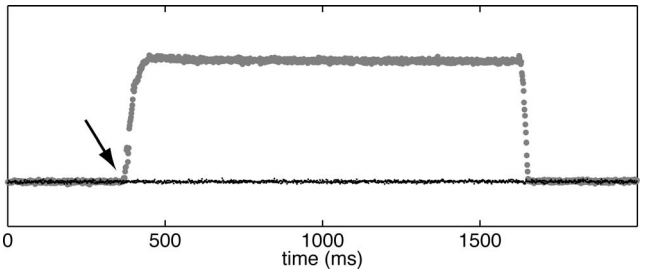

Fig. 1 Excitation light synchronization. Initially, both cyan and royal blue on-intensity is set to 0. When blue on-intensity is turned up (arrow), light collected during cyan frames (black dots) remains at baseline, while light collected during alternating blue frames (gray circles) is elevated.

We confirmed accurate light switching at the beginning of each mapping experiment in a similar way by setting one color's on-state intensity to 0 and recording fluorescence elicited by the other color in alternating camera frames. This was repeated with the colors swapped. We ensured that the camera detected no measurable fluorescence during dark frames in either case.

2.2 *Experimental Procedure*

Five domestic farm pigs of either sex weighing 32 ± 13 kg were studied. The heart isolation and Langendorff perfusion protocol is described in detail elsewhere.[4] Briefly, the animals were anesthetized and their hearts rapidly excised and placed in ice-cold saline solution. The hearts were cannulated through the aortic root and perfused with chilled modified Tyrode's solution. Black polyethylene markers were attached to the cold anterior left ventricular epicardium with black cyanoacrylate adhesive (Loctite #426). The markers were 0.25-mm thick and 4 mm in diameter with a 2.5-mm diameter hole. They were fabricated by punching two concentric holes in a polyethylene plastic sheet with coring tools (Harris Unicore). After attaching the markers, the hearts were suspended from the aorta and perfused at a constant rate of 200 ml/min with warm (37°C) oxygenated modified Tyrode's solution. To minimize rigid-body swinging and twisting movement of the beating heart, two 22 gauge, 5/8 in. needles were inserted into each ventricle near the apex, approximately in plane with the camera's view, and clamped in space. In two

preparations, a Tyrode's filled balloon connected to a loading column (~10 cm-H_20) was inserted into the left ventricle. The CCD camera lens was positioned within 10 cm of the heart. Hearts were stained with VSD by delivery of three successive 10 ml, 15 μm/l boluses of di-4-ANEPPS solution (Sigma) into the cannula. Droplets of perfusate, which gradually collect on the markers, were blotted with gauze just before each optical recording.

In 3 of the 5 hearts (termed the "optical-only" group), we performed the following protocol: While beating, each heart was optically mapped during steady state bipolar pacing from the right ventricle (RV) at the following intervals: 700, 500, 400, 300, and 250 ms. After all beating-heart recordings were completed, contraction was arrested by adding butanedione monoxime to the perfusate (BDM; 20 mmol/l, Sigma) and hearts were optically mapped during pacing at the same intervals listed above. We then optically mapped the BDM-treated hearts during 300 and 500 ms pacing while swinging the heart on its cannula. All recordings were 6 s long at 700 fps (350 fps per excitation light color).

In the remaining two hearts (the "optical + electrical" group), we used a floating microelectrode to record V_m from a single site simultaneously with the optical recordings. Microelectrodes (10 to 30 MΩ tip resistance, filled with 3 M KCl) were prepared as described elsewhere[17] and positioned adjacent to an epicardial marker (within 2 mm). They were not positioned within markers because that would have obscured the optical signals. The microelectrodes were mounted on fine springs to follow cardiac motion. The electrical signal was amplified using a capacitance-compensation preamplifier (model 773, WP Instruments), sampled at 8 kHz, and recorded on a custom-made cardiac mapping system. The CCD camera's "shutter" signal was fed to a separate channel of the mapping system to guide offline time-alignment of the electrical and optical recordings. We made simultaneous electrical/optical recordings from beating hearts during steady-state bipolar pacing from the RV at 400 and 500 ms intervals.

2.3 *Data Analysis*

All data analyses were performed in MATLAB (version 2009b, Mathworks). Where appropriate, MATLAB functions are identified.

2.3.1 *Creating binary marker masks*

Approximate initial positions of all markers were manually selected in the first frame of each recording. For each marker, a sub-image of the first camera frame containing only that marker [Fig. 2(a)] was resampled at 4 times (4×) the original camera resolution using cubic interpolation [imresize(), Fig. 2(b)]. Edges of the 4× resampled image were found using canny edge detection [edge(), Fig. 2(c)]. Small gaps in the identified inner and outer edges of the marker were closed by morphological dilation [imdilate(), Fig. 2(d)]. A flood-fill operation was applied to the center of the sub-image to detect the region bounded by the marker's inner edge [imfill()]. The flood-filled region was smaller than the true size of the hole in the marker because of the edge-closing dilation operation; to compensate, the flood-filled region was dilated [Fig. 2(e)]. The mask of the inner marker region was further dilated and subtracted from the dilated edge image to yield a dilated edge image with the inner ring removed [Fig. 2(f)]. A second flood-fill operation was applied to the center of the remaining edge image to find the region bounded by the marker's outer edge, and the resulting outer-edge region was also dilated to correct for the initial gap-closing edge dilation [Fig. 2(g)]. Subtraction of the inner-edge region from the outer-edge region produced a binary mask of the marker [Fig. 2(h)]. We resampled the resulting mask to give a resolution of 8× the original camera resolution. Figure 2(i) shows an 8× resampling of the original sub-image with overlay of the contours of the final resampled binary marker mask.

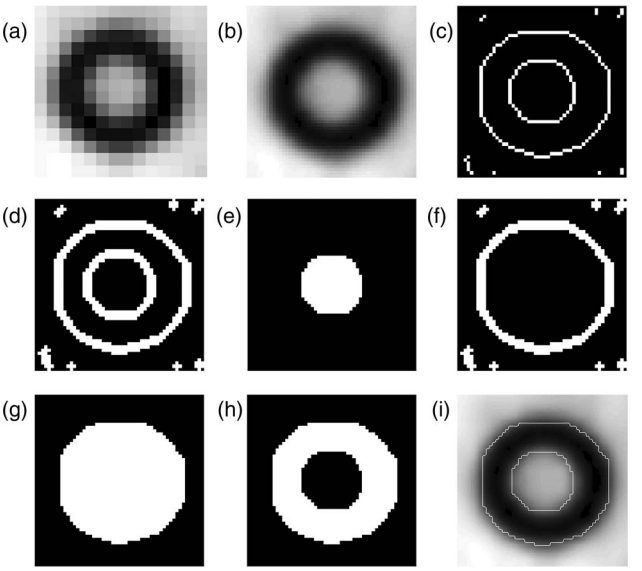

Fig. 2 Binary mask creation for tracking an epicardial marker through frames of video. (a) Original subimage of one marker. (b) 4× resampling of image in (a) (bicubic interpolation). (c) Edges of image in (b) detected with Canny edge detection. (d) Morphological dilation closes any gaps in the inner and outer edges of the marker. (e) A flood-fill operation is applied to the center of the image in (d). The area identified by flood-fill is then dilated to compensate for the dilation performed in (d). (f) Subtraction of a dilation of the image in (e) from the image in (d) yields a dilated edge image with the inner ring removed. (g) Flood-fill identifies the outer edge of the marker. The area identified by flood-fill is then dilated to compensate for the dilation performed in (d). (h) Subtraction of the image in (e) from the image in (g) gives a binary mask of the marker. (i) The mask binary mask in (g) is resampled to the image resolution used for motion tracking (8× original camera resolution). The white lines show the inner and outer contours of the resampled binary marker mask, overlaid on an 8× resampling of the original sub-image.

2.3.2 *Tracking markers*

We tracked marker motion using two-dimensional (2D) cross-correlation to find the best alignment of the marker mask with the imaged marker in each subsequent frame of video. For each marker, a sub-image of the raw camera frame was selected and resampled at 8× to match the resolution of the binary marker mask. For accurate tracking, the sub-image must be larger than the binary mask by enough pixels to bound the largest movement of the marker between successive video frames. Furthermore, to avoid resampling artifacts due to edges, the sub-image must be large enough that markers never reach its edge. To achieve this, marker sub-images were the size of the marker's binary

mask, padded by 4 pixels in both directions, and centered on the marker position from the previous frame. Sub-images were typically 14 × 14 pixels.

Markers were tracked as follows: Starting with the first frame of video, 2D cross-correlation [normxcorr2()] identified the best alignment of the marker mask with the resampled sub-image. The position of the marker in the first frame of video was recorded as the *X-Y* coordinates of the center of the aligned marker mask. The recorded *X-Y* marker coordinate in the first frame of video defined the center for sub-image selection in the second frame of video. Then, 2D cross-correlation identified the best alignment of the marker mask with the resampled sub-image from the second frame of video. The marker position in the second frame of video was recorded as the *X-Y* coordinates of the center of the aligned marker mask. This procedure was continued for all frames of video.

2.3.3 *Sampling fluorescence from moving markers*

The fluorescence emitted by the tissue enclosed by each moving marker was collected by dilating the cross-correlation–aligned binary mask of the inner-ring region and multiplying it by an 8× resampled sub-image of the marker. The mask was dilated to cause the binary mask to overlap the inside edge of the material marker. This ensured that the encircled tissue region was still completely sampled in the presence of small errors in motion tracking. The signal associated with each camera frame was the average intensity of pixels in the marker image after applying the mask. The royal blue- and cyan-illuminated frames were deinterlaced to yield two temporal signals for each marker, each sampled at 350 Hz. Although marker positions were known continuously through every frame of video, the mask for acquiring the fluorescence signal was only repositioned after even-numbered frames of video. This ensured that the same masked region was sampled for corresponding royal blue- and cyan-illuminated frames.

2.3.4 *Excitation ratiometry for estimating V_m*

In conventional optical mapping, the patch of tissue imaged by a particular photodetector pixel changes if the heart moves. Because effective dye concentration and electrical activity are spatially heterogeneous, motion therefore introduces an artifact in a pixel's signal that is large enough to swamp out the V_m signal. This is why conventional optical mapping experiments usually employ an electromechanical uncoupling agent. By collecting a signal from marked tissue, we eliminate these sources of motion artifact. However, we also introduce a new one: Because the excitation light is not perfectly uniform, as the marker moves, change in local light intensity becomes mixed into the V_m signal as artifact.

We employ a variant of our recently developed excitation ratiometry technique[18] to remove this artifact. Fluorescence elicited by cyan (505 nm) excitation light and recorded in the 605 ± 25 nm band is inversely sensitive to membrane potential.[18] Cyan-elicited signals therefore contain inverted action potentials polluted with motion artifact. In contrast, because the wavelength band admitted by our emission filter is near the isosbestic point for royal blue (450 nm) excitation,[18] royal blue excitation produces fluorescence that is effectively insensitive to voltage. Thus, blue-elicited signals are primarily indicative of the changing excitation light intensity the marker encounters as it moves (i.e., motion artifact).

The signal at a photodetector pixel due to cyan excitation can be modeled as $S_c = I_c(B_c\text{-}V_m)M + c$, where I_c is the intensity of cyan illumination, B_c is the constant background fluorescence (a function of local effective dye concentration), V_m is the membrane-potential–induced fluorescence signal, M is the artifact signal (primarily due to motion), and c is a constant offset (the signal present when the photodetector is not exposed to light—this is a property of the imaging hardware). Similarly, the blue-elicited signal can be expressed as $S_b = I_b B_b M + c$. Note that V_m is absent from S_b and M is common to both S_c and S_b. Subtracting c and dividing S_b by S_c gives

$$R_{cb} = \frac{S_b}{S_c} = \frac{I_b B_b}{I_c(B_c - V_m)}. \tag{1}$$

Because V_m is much smaller than the background fluorescence, we can use the power series approximation $1/(1-x) \approx 1+x$ (valid to first order for $-1 < x < 1$) to obtain

$$R_{cb} \approx \frac{I_b B_b}{I_c B_c}\left(1 + \frac{V_m}{B_c}\right). \tag{2}$$

Thus, common artifact is removed from the ratio signal and the result is proportional to the membrane potential with a constant offset. As noted above, most of the common mode artifact is likely due to motion through a nonuniform light field, but there may also be contributions from local contraction of the tissue surrounded by the rings. The offset and proportionality constants in Eq. (2) are functions of the *ratio* of two excitation light intensities. For complete artifact removal, this ratio should be constant over the spatial trajectory of a marker, even if the intensities themselves are not.

Filtering of excitation light was necessary because both the cyan and the royal blue LEDs emit some red (>580 nm) light that can cause specular reflection highlights on the wet epicardial surface. These reflections do not cancel ratiometrically because the cyan LEDs have a larger red component than the royal blue LEDs.

We computed activation times as local maxima in the 9-point derivative of a 21-point, fifth-order Savitzky–Golay filtered signal [sgolay()].[19] We computed the second derivative with a 41-point quadratic Savitzky–Golay filter and identified repolarization times in each signal as local maxima in the second derivative of V_m.[20] Action potential duration (APD) was the time between activation and repolarization for each action potential in each signal.

2.3.5 *Measuring epicardial deformation*

Given the coordinates of three material points on a deformable surface in both undeformed and deformed configurations, the deformation can be quantified using homogeneous finite strain theory, which yields a two-dimensional strain tensor that is assumed to be constant within the region enclosed by the markers.[7] We obtained an estimate of epicardial deformation due to contraction by computing strain from the *X-Y* coordinate trajectories of the material markers in the plane of the CCD camera frame. Because the 2D camera frame was used as the coordinate

system for this measurement, our strain measurements neglect any motion in or out of the camera frame.

Local triples of markers were selected for strain measurement by a Delaunay triangulation of the markers [delaunay()]. We computed 2D homogeneous finite strain for each resulting triangle using the method of McCulloch et al.[21] Briefly, in this method, the deformation gradient tensor, **F**, relates an arbitrarily short line segment in the reference ($d\mathbf{x}$) and deformed ($d\hat{\mathbf{x}}$) states according to the equation: $d\hat{\mathbf{x}} = \mathrm{F}d\mathrm{x}$. **F** is determined from two 2D line segments defined by the three marker coordinates of each epicardial triangle. **F** is decomposed into a rigid body rotation component, **R**, and a stretch tensor, **U**. The largest eigenvalue of **U** is the major principal strain for the region enclosed by the three points.

Others have defined the reference state as the conformation of the markers at end-diastole, defined by the time of the *R* wave in the electrocardiogram.[7,8] Following that convention, we define the time of end-diastole for each beat as the average activation time at the three vertices of each epicardial triangle. Strain tensors were computed for each frame during systole using the previous end-diastolic conformation as the reference state. We report the eigenvalue of each strain tensor (principal strain) that corresponds to maximal shortening.

3 Results

3.1 *Optical-Only Hearts*

In the three optical-only hearts, 17, 14, or 13 markers were attached to the epicardium [Fig. 3(a)]. Of these, 9, 9, or 6 markers were nominally in the plane of the camera frame and were used for further analysis.

Figure 4(a) shows the raw fluorescence signal collected from the tissue surrounded by one ring during pacing (700 ms interval). No BDM was present and the heart was contracting vigorously. The royal blue- and cyan-elicited signals are interlaced in time. Figure 4(b) shows the two signals after de-interlacing. Figure 4(c) is the ratio of the signals, which estimates V_m. Action potentials with nearly normal morphology are clearly present and most motion (and other common-mode) artifact has been cancelled. After an arresting motion with BDM, action potentials with normal morphology were clearly visible in the cyan-elicited signals without the need for ratiometry. As in conventional optical mapping, the action potentials were inverted with voltage sensitivity, expressed as the fluorescence change due to an action potential relative to the background fluorescence ($\Delta F/F$), of ~4%. In contrast, the royal blue-elicited signals were nearly insensitive to V_m. By averaging multiple beats, inverted action potentials could be seen ($\Delta F/F \sim 0.2\%$), but their amplitudes were generally well below the noise level.

V_m signals obtained from 9 markers on the beating heart shown in Fig. 3(b) are shown in Fig. 5(a) (500 ms pacing) and in Fig. 5(g) (300 ms pacing). In the corresponding Figs. 5(d) and 5(j), we characterize the motion of the markers by tracking the distance between each marker and the origin of a 20 × 20 pixel subimage containing the marker. As in Fig. 4, motion artifact is greatly reduced by excitation ratiometry, but some motion artifact is still evident in the V_m signals.

V_m signals obtained from the stationary heart after BDM treatment are shown in Figs. 5(b) and 5(h) (500 and 300 ms pacing, respectively). The corresponding marker displacement plots in Figs. 5(e) and 5(k) confirm that motion was almost completely abolished. V_m signals obtained from BDM-treated hearts swinging on the cannula are shown in Figs. 5(c) and 5(i) (500 ms and 300 ms pacing, respectively). In these recordings, motion [Figs. 5(f) and 5(l)] had similar amplitude as in the beating-heart recordings, but was not synchronized with the electrical rhythm. The motion produced by swinging the heart on the cannula consists of translation of the heart in space, roughly in the plane of the camera's view, and should not affect electrophysiology. Thus, we expect action potential morphology when comparing Figs. 5(b) to 5(c) and Figs. 5(h) to 5(l) to be very similar, which was the case. Videos 1 and 2 are recordings of 500 ms pacing in a beating and BDM-treated swinging heart, respectively.

In each recording, mean APD was computed as the average APD of all action potentials in all of the estimated V_m signals.

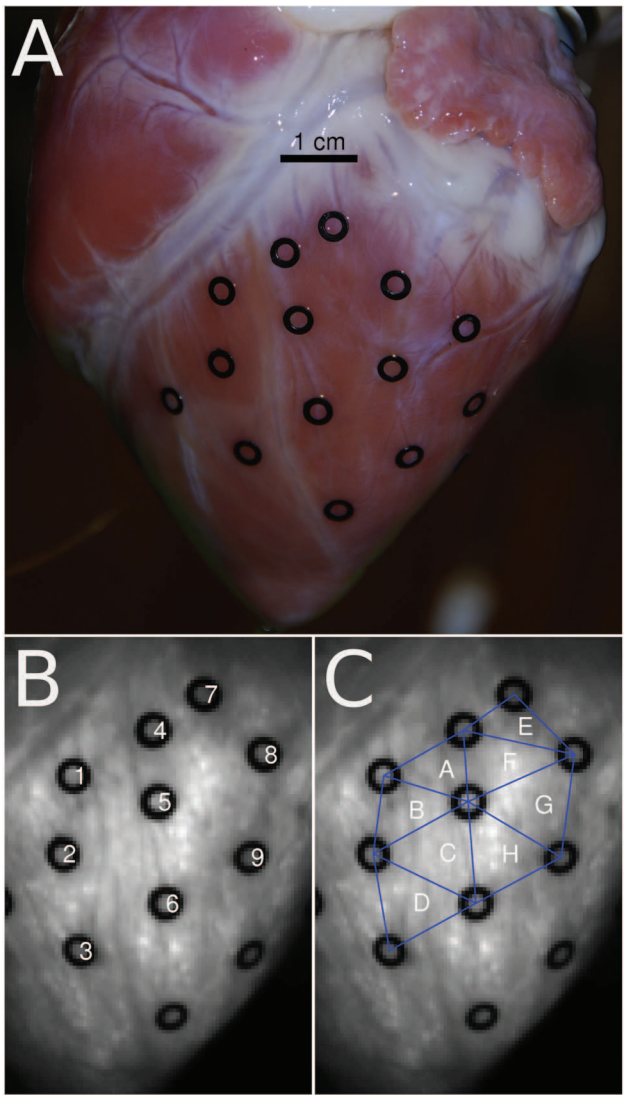

Fig. 3 Ventricular markers. (a) Heart with 14 markers attached with cyanoacrylate adhesive gel. (b) One frame of CCD camera video. Local V_m signals are obtained from the fluorescence emitted from inside each marker. Marker numbers correspond to action potential traces in Fig. 5. (c) Triples of markers define regions for strain measurements. Triangles, lettered A–H, correspond to major axis strain plots in Fig. 7.

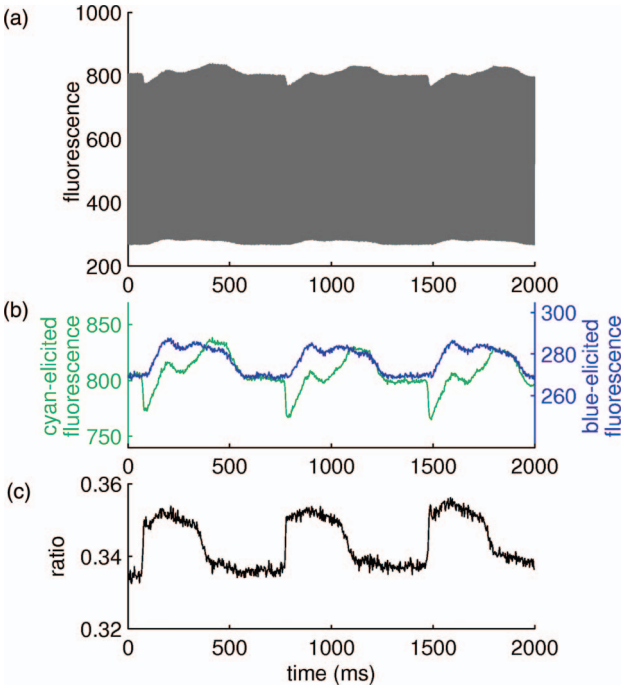

Fig. 4 Excitation ratiometry. (a) Time-interlaced fluorescence signal obtained from a single marker tracked through frames of CCD video. Signal is from marker number 5 in Fig. 3(b) during 700 ms bipolar pacing. (b) De-interlaced signals, corresponding to alternating frames of cyan and royal blue excitation. (c) Common artifacts in the two fluorescence signals (primarily motion) are attenuated in the ratio signal. Fluorescence units are analog-to-digital conversion counts. No temporal filtering was applied to these signals.

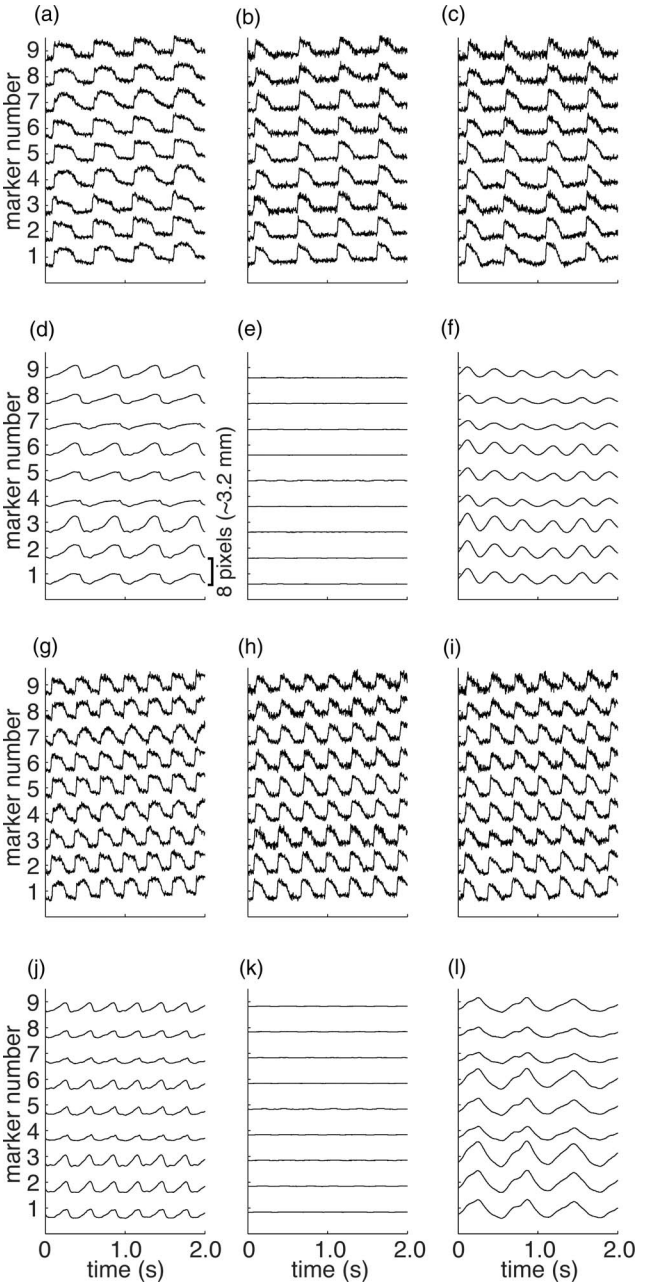

Fig. 5 (a)–(c) Fluorescent action potential signals obtained from all numbered markers in Fig. 3(b) during 500 ms bipolar pacing for (a) beating, (b) BDM-treated stationary, and (c) BDM-treated swinging heart recordings. (d)–(f) Relative marker displacement during the mapping runs in (a)–(c). Displacement was computed as the distance from the marker to the origin of a 20 × 20 pixel region containing the marker. (g)–(l) Fluorescent action potential signals obtained from the same numbered markers during 300 ms bipolar pacing for (g) beating, (h) BDM-treated stationary, and (i) BDM-treated swinging heart recordings. J-L(j)–(l) Relative marker displacement during the mapping runs in (g)–(i). Displacements are computed in the same manner as for (d)–(f). The calibration bar in (d) applies to all displacement traces. No temporal filtering was applied to these signals. (The recordings of 500 ms pacing in beating and BDM-treated swinging conditions are also shown in Videos 1 and 2, respectively.)

Mean APDs for beating and stationary BDM-treated hearts are shown in Fig. 6(a). For each pacing rate, a one-sided paired t-test, using paired APD measurements at individual spots before and after delivery of BDM ($n = 24$ markers in 3 hearts), indicated that APD was significantly shortened by BDM ($p < 10^{-14}$ for all the previously listed pacing rates). This is expected, as APD shortening is well documented in BDM-treated myocardium.[22] In contrast, if our method successfully removes motion artifact, we expect APD in BDM-treated stationary hearts to be the same as APD in BDM-treated moving hearts (hearts swinging on the cannula). A two-sided paired t-test compared APD at individual markers between stationary and swinging states across all hearts ($n = 24$ markers in 3 hearts). APD during swinging did not significantly differ from stationary APD at either recorded pacing rate ($p = 0.83$ for 500 ms and $p = 0.85$ for 300 ms). APDs in swinging and stationary BDM-treated hearts at both 500 and 300 ms rates are shown in Fig. 6(b).

We computed apparent epicardial strain for triangular regions of epicardium bounded by local triples of epicardial markers [Fig. 3(c)]. Delaunay triangulation of the markers produced 8, 8, or 4 triangular regions, respectively, for the three hearts studied. For each beat, 2D homogeneous finite strain was computed at each time sample for each triangle using the end-diastolic conformation of the markers as the undeformed reference state. Figures 7(a) and 7(b) show the principal strain corresponding to the greatest shortening for all triangles in the heart shown in Fig. 3(a) during 500 ms and Figs. 3(b) during 300 ms pacing. Peak per-beat shortening from all mapped beats in all triangular faces from the three hearts was significantly greater for 500 ms pacing than 300 ms pacing (5.8 ± 1.8% versus 4.4 ± 1.6%; $p < 0.01$). Spatial distributions of peak shortening

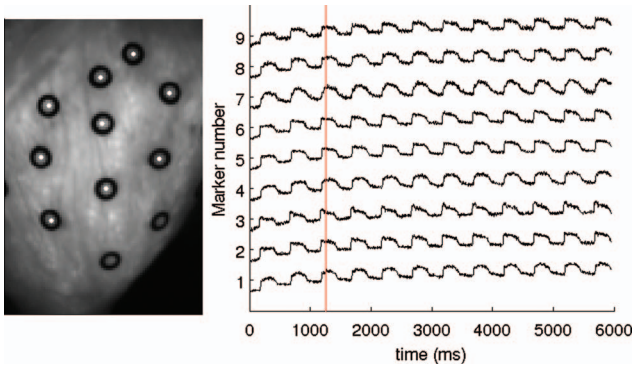

Video 1 Optical mapping of 500 ms pacing in a beating heart. V_m traces are shown for the 9 numbered markers in Fig. 3(b). A vertical red line shows the current video position in time. White dots indicate depolarization and repolarization of the tissue encircled by each marker. Frame rate is 1/10 real time. Only cyan frames are shown. Activation wavefronts are visible as slightly darker shadows propagating across the heart. (MPEG, 9.3 MB) [URL: http://dx.doi.org/10.1117/1.3630115.1].

across the marker triangles are shown in Figs. 7(c) and 7(d) for 500 and 300 ms pacing, respectively.

3.2 *Optical + Electrical Hearts*

In the first optical + electrical heart, we made 7 simultaneous optical/microelectrode V_m recordings from 3 different marker rings. In the second heart, we made 4 recordings from 3 different marker rings. In each case, the floating microelectrode was positioned within 2 mm of the corresponding marker.

An example of simultaneously recorded electrical and optical signals is shown in Fig. 8. Figure 8(a) shows the individual cyan- and blue-elicited optical signals and indicates that substantial artifact is present. Figure 8(b) is the ratio V_m signal, and Fig. 8(c) is the microelectrode recording. Because the rapidly switching LED driver circuit interfered with the microelectrode recordings, and the microelectrode equipment interfered with positioning of the excitation light sources, both optical and electrical signals are noisy. Consequently, all simultaneously recorded electrical and optical signals were filtered with a 5-point averaging filter followed by an 11-point median filter. Activation and repolarization times were then computed as previously described.

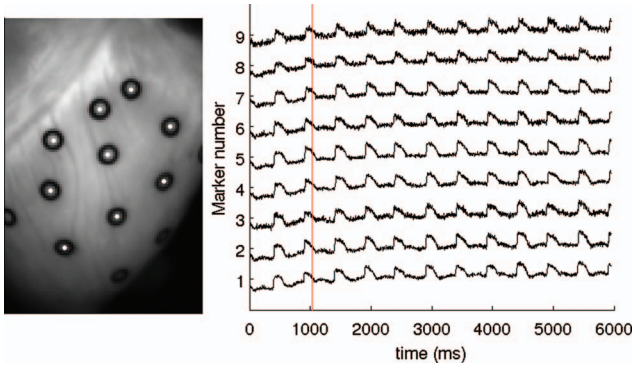

Video 2 500 ms pacing in a BDM-treated swinging heart. Video layout is the same as in Video 1. (MPEG, 9.3 MB) [URL: http://dx.doi.org/10.1117/1.3630115.2].

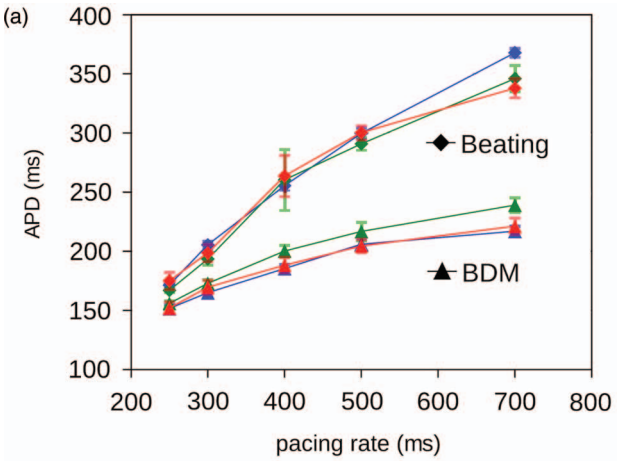

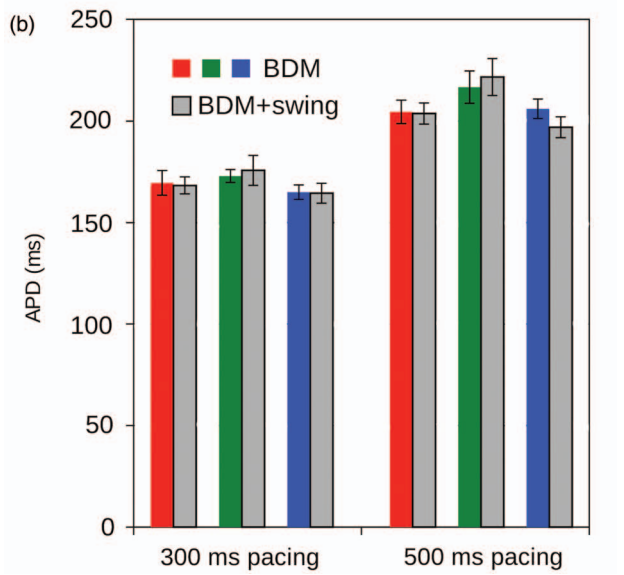

Fig. 6 Action potential durations. (a) APD in beating and BDM-treated (stationary) recordings. At each pacing rate, APDs for all markers are averaged to give a single APD value for each recording. Measurements that are common to a single heart are connected by lines. Error bars show standard deviations. APDs differed significantly for beating and BDM recordings at each pacing rate. (b) APD in stationary and swinging BDM-treated heart recordings. APDs for corresponding hearts are paired. APD values did not differ significantly between stationary and swinging conditions.

To determine if the measured activation times were the same for both electrical and optical recordings, the difference in activation times was computed for each beat ($t_{\text{act\_optical}} - t_{\text{act\_electrical}}$). In all optical + electrical recordings, the mean difference in activation time was -1.0 ± 6.8 ms. This small difference did not differ significantly from 0 (t-test on the population of 134 beat-wise differences, $p = 0.08$). Figure 8(d) (black bars) shows a histogram of the activation time differences. Almost all differences were less than 15 ms, which is on the order of the upstroke duration for action potentials recorded optically from a sub-millimeter epicardial region.[23] Optical upstroke durations in our data were typically even longer than this because each signal integrated information from a 2.5-mm diameter epicardial region. APDs were compared between optical and electrical

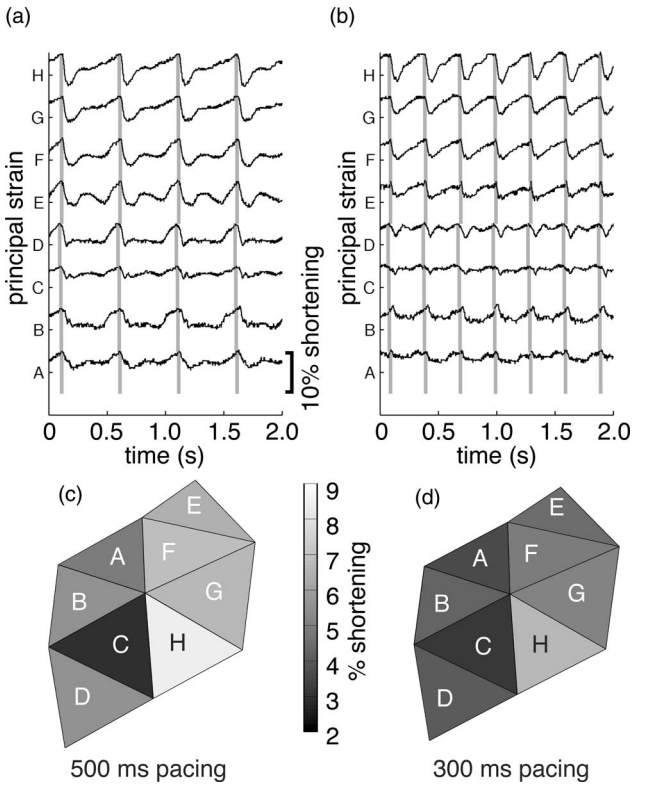

Fig. 7 (a) and (b) Maximum principal finite strain measured in the camera's view plane for each triangle (A–H) shown in Fig. 3(c). Gray bars indicate time of end-diastole, identified by the average activation time for the three vertices of each triangle. The calibration bar applies to all traces. (a) 500 ms pacing. (b) 300 ms pacing. Spatial distributions of peak shortening for 500 ms (c) and 300 ms (d) pacing.

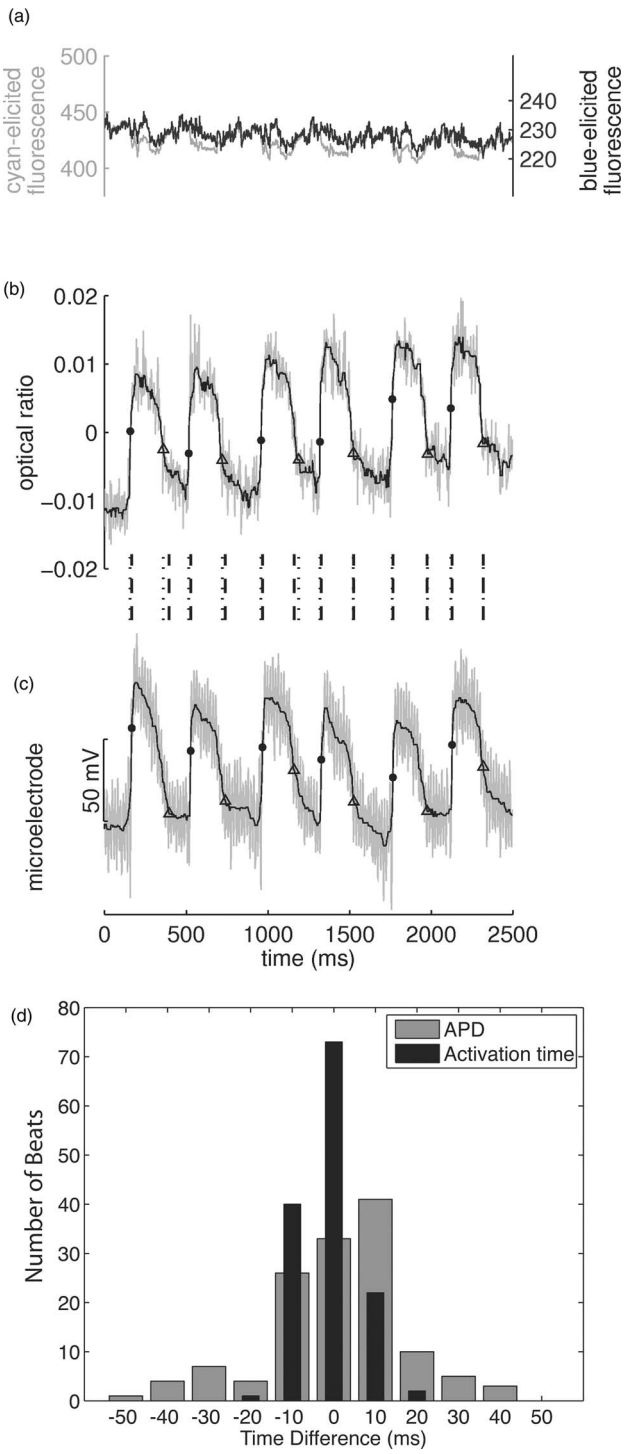

Fig. 8 Simultaneous optical and floating microelectrode data. (a) shows the individual cyan- and blue-elicited optical signals recorded from a single epicardial marker during 400 ms pacing. (b) is the corresponding ratio signal and (c) is the simultaneously recorded microelectrode signal. The signals in (b) and (c) are filtered by 5-point smoothing followed by 11-point median filtering. Unfiltered signals are gray and filtered signals are black. Dots and triangles indicate depolarization and repolarization times, respectively. Vertical lines between (b) and (c) show the relative timing of depolarization/repolarization events in the two signals (dotted lines correspond to the optical signal, dashed lines correspond to the electrical signal). (d) Shows histograms of the differences in activation time (black) and APD (gray) between optical and electrical signals for all recorded beats. Bins are 10 ms wide.

recordings in the same manner. The difference in APD for each beat ($APD_{optical} + APD_{electrical}$) was 1.3 ± 16.6 ms [Fig. 8(d), gray bars]. Again, this was not significantly different from 0 (t-test on the population of 134 beat-wise differences, $p = 0.37$). These data demonstrate that the method reconstructs V_m signals in freely contracting myocardium.

4 Discussion

We demonstrate a method to record optical membrane potential signals while simultaneously quantifying mechanical deformation across a large epicardial region in beating hearts. In this study, we placed only a few markers and therefore measured V_m with relatively low spatial resolution. However, much higher resolution can be achieved simply by using more, possibly smaller, markers.

This method improves the physiological relevance of optical recordings because electromechanical uncoupling agents are not required. The electrophysiological impact of such agents is well known: Some electromechanical uncouplers interfere directly with ion channels (e.g., BDM, cytochalasin-D).[4] However, even if an uncoupling agent is free of direct electrophysiological effects, the absence of contractions will diminish the flow of interstitial fluid out of the muscle, gradually causing the heart to become edemic.[24] This can affect electrophysiology by modulating the activity of swelling-activated channels.[25]

4.1 *Motion Tracking*

The tracking marker position in each frame of a video is the most time consuming step in processing our beating heart data. It may be possible to accelerate this process by tracking marker position in fewer frames and using known marker positions to estimate the marker position for the skipped frames. Video-based strain measurement techniques typically record marker positions at much slower rates than the 700 fps rate used in this study [for example, 50 (Ref. 13) or 120 (Ref. 26) fps in dog hearts]. An even more efficient approach might use an adaptive algorithm to increase the marker tracking time step when the marker displacement between frames is small, and to decrease the marker tracking time step over intervals when the marker displacement is larger.

4.2 *Motion Artifact and Ratiometry*

Classically, motion artifact results largely from a loss of correspondence between a photodetector pixel and the tissue. Because the desired fluorescent V_m signal is small ($\Delta F/F \sim 4\%$ in our cyan excitation data), even small artifacts are large enough to mask the V_m signal. Our method eliminates this type of motion artifact by tracking marker position and using the fluorescence from the encircled patch of tissue as an estimate of V_m. However, it introduces a different form of motion artifact caused by changes to a marker's baseline fluorescence as it moves across a nonuniform excitation light field. A highly uniform excitation light field would minimize this type of motion artifact, but is difficult to achieve in practice.

Ratiometry is often used to reduce the magnitude of motion artifact in optical signals.[27,28] In cardiac tissue, ratiometry typically employs a single excitation wavelength, and simultaneously records two separate emission bands. When VSD-stained tissue depolarizes, the spectrum of emitted fluorescence shifts to shorter wavelengths, causing green emission to increase and red emission to decrease. Thus, action potentials in the green and red signals have opposite polarity. Taking the ratio of the signals (emission ratiometry) reinforces action potentials while canceling the common artifact.

In contrast, we employed excitation ratiometry, which relies on the voltage dependence of the VSD's excitation spectrum. We exposed the VSD-stained tissue to two different colored light sources, and recorded emitted fluorescence for a fixed emission band. This excitation-ratiometric approach was first demonstrated by Montana and colleagues,[29] who rapidly alternated the color of excitation light with a 400 Hz chopper. Our technique employs the same principle, but rapid light switching is achieved by pulsing high powered LEDs in synchrony with CCD camera frames. An important advantage of excitation ratiometry is that it requires only one photodetector: emission ratiometry requires two photodetectors with optics carefully aligned so that corresponding pixels image the same tissue. The polarity and amplitude of voltage-sensitive fluorescence can be controlled by carefully choosing the wavelengths at which tissue is excited and fluorescence is recorded (see Ref. 18 for discussion). Our spectral scheme was designed to maximize the voltage sensitivity of one excitation color (cyan) and minimize it with the other (royal blue). The near absence of V_m information in the royal blue-elicited signal means that it can potentially be used as a reference signal for co-local optical recordings of other parameters. One drawback of excitation ratiometry is that it halves the effective temporal resolution of the photodetector. Another is that depending on the particular spectral design, it may require a narrower emission band than other methods, which limits light reaching the photodetector and degrades the signal-to-noise ratio. This can be compensated for by increasing excitation light intensity.

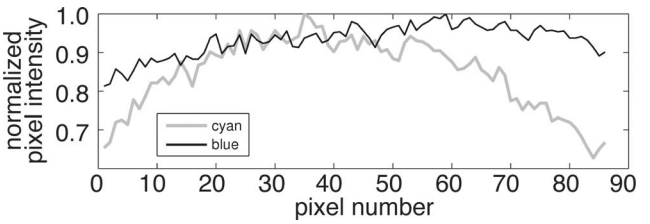

Fig. 9 Illumination profile across one row of pixels during cyan (gray line) and royal blue (thin black line) illumination of a flat paper target. Royal blue illumination is more uniform.

Excitation ratiometry corrects for motion artifact due to spatially nonuniform illumination if the intensities of the two excitation light colors are related everywhere by the same constant. Because this is approximately true with our excitation light setup, motion artifact is substantially reduced in the ratio of the royal blue to cyan signals. However, there are residual differences in the royal blue and cyan illumination fields that we believe are responsible for the motion artifact that remains in our V_m signals. Figure 9 shows the intensity profile of cyan and royal blue excitation light reflected from a piece of white paper. The cyan light drops off away from the center of the image while the royal blue light field is more uniform. The difference is largely a result of the excitation light filtering scheme: The cyan LED output (505 nm peak, 30 nm half-width) is near the 525 nm shortpass cutoff of our excitation light filters (480 ± 45 nm bandpass). At a 90 deg angle of incidence, the majority of the cyan LED output passes through the filter. However, the cutoff of the shortpass interference filter shifts to a shorter wavelength for light that hits the filter at an angle less than 90 deg.[30] As a result, each filtered cyan LED produces a spot that is bright in the center and dim around the edges. This vignetting effect is smaller during royal blue excitation because the royal blue LED output (450 nm peak, 24 nm half-width) is further from the shortpass cutoff. In general, markers in the center of the field of view are less affected by cyan light vignetting and exhibit less motion artifact [markers 5 and 6, Figs. 4(a) and 4(g)], while markers closer to the edges of the camera frame exhibit more motion artifact (marker 7). One way to reduce the difference between the light fields for the two colors would be to collimate the LED output prior to shortpass filtering.

Another factor that could have contributed to the remaining motion artifact in our data is wavelength-dependent light transmission and diffraction. Brandes et al.[31] identified these effects on emitted fluorescence as a potential source of error in their emission ratiometry experiments. Our experimental setup could admit similar error due to wavelength-dependent transmission and diffraction of excitation light around the edges of the markers and through the muscle.[32]

4.3 *Strain Measurement*

Because we used only one camera, the true distances between points on the three-dimensional (3D) epicardial surface were not known but were approximated as the 2D distance between marker coordinates in the 2D camera frame. Any marker movement toward or away from the camera produced erroneous scaling (growing or shrinking) of the distances between the markers. We minimized this error to some degree by stabilizing out-of-plane motion of the heart with needles and by mapping from regions that were relatively flat and parallel to the camera plane. Additionally, spherical aberration of the camera lens can introduce error in distance measurement, and we did not correct for this effect. As a result, our strain measurement technique produces only an approximation of true epicardial strain. Strain could be measured more accurately by imaging each marker with two cameras and using binocular vision principles to reconstruct marker positions in 3D. This scheme has been employed by others to measure strain at slower video rates.[21,26] Additionally, strain within marker triangles is only approximately constant. By fitting a finite element model to the marker positions in the reference and deformed configurations, continuous strains can be computed across the entire mapped region.[26]

4.4 *Comparison to Other Methods*

Seo et al.[16] recently employed a marker tracking scheme together with optical mapping to estimate strain distributions and track electrical propagation in cardiac preparations. For each video frame, they used a cross correlation technique similar to ours to find the displacements of epicardial markers relative to a reference video frame. The displacements were used to estimate epicardial strain and also to find an affine transformation (combination of rotation, translation, shear, and/or scale) that optimally mapped the marker positions from the reference frame to the deformed frame. This motion model, together with two-camera emission ratiometry, was used to reconstruct V_m across the field of view. Other investigators have also used affine transformations to model motion from frame-to-frame. However, instead of tracking discrete markers, transformations were found to maximize a global measure of similarity based on intrinsic image features.[33,34] A key difference between our method and that of Seo et al. is that we do not rely on a global linear transformation to track tissue points from frame-to-frame. Such a motion model may not reliably compensate for large nonlinear deformations or for motion across large regions.[33] By using ring-shaped markers, we directly track the tissue generating the V_m signal and avoid this source of error. Another important difference is that by using excitation rather than emission ratiometry, our method requires only a single camera.

In another recent method introduced by Bagwe et al.,[35] each video frame is divided into a grid of sub-images. For each sub-image, a local displacement is found that best matches its intensity pattern with local features of the reference frame. The displacement vectors are then interpolated to generate a displacement field defined at each pixel. This displacement field combined with emission ratiometry is used to construct the V_m field. This method was used only for motion artifact correction and not for quantifying epicardial deformation. The most important difference between the Bagwe et al. method and ours is the use of markers. We believe that the marker approach is more robust because tissue tracking from frame-to-frame is unambiguous: markerless sub-images may lack distinct features, and features that do exist may change with time because of voltage-sensitive fluorescence changes and changes in local illumination patterns as the heart moves. In addition, the use of markers enables a relatively straightforward extension of motion tracking to three dimensions through the use of dual cameras (i.e., binocular vision). Because of the difficulty of identifying the same epicardial point in two camera views in the absence of markers, markerless motion tracking will likely remain limited to motion in the plane of the camera. Unlike the Bagwe et al. method, we have not implemented an interpolation scheme to estimate the displacement field over the entire mapped region. However, doing so would be a natural extension of our method and would increase the spatial resolution of the V_m recordings beyond that defined by marker density, although with a possible cost in motion tracking accuracy away from markers.

4.5 *Potential Applications*

In addition to allowing optical mapping of V_m in the absence of electromechanical uncoupling agents, by enabling simultaneous measurement of V_m and epicardial deformation, the new method could provide insight into a number of pathologies and therapies that inherently involve the interplay between mechanical and electrical parameters. Examples include precordial thump,[36,37] commotio cordis,[38] electromechanical dissociation following resuscitation,[39] pacing schemes for cardiac resynchronization therapy,[40] and the interplay between mechanical stretch and wave propagation during tachyarrhythmias and defibrillation.

Acknowledgments

This work was supported in part by NSF Grant No. CBET 0756117, NIH Grant No. HL64184, and AHA Grant No. 10GRNT4280098. We thank Frank Vance and Julia Todd for their help with animal preparation.

References

1. M. Shenasa, G. Hendricks, B. Borggrefe, and G. Breithardt, *Cardiac Mapping.* 3rd Ed., Blackwell Publishing, Oxford, United Kingdom (2009).
2. I. R. Efimov, V. P. Nikolski, and G. Salama, "Optical imaging of the heart," *Circ. Res.* **95**, 21–33 (2004).
3. V. Fedorov, I. Lozinsky, E. Sosunov, E. Anyukhovsky, M. Rosen, C. Balke, and I. R. Efimov, "Application of blebbistatin as an excitation-contraction uncoupler for electrophysiologic study of rat and rabbit hearts," *Heart Rhythm* **4**, 619–626 (2007).
4. H. Qin, M. W. Kay, N. Chattipakorn, D. T. Redden, R. E. Ideker, and J. M. Rogers, "Effects of heart isolation, voltage-sensitive dye, and electromechanical uncoupling agents on ventricular fibrillation," *Am. J. Physiol. Heart Circ. Physiol.* **284**, H1818–H1826 (2003).
5. N. B. Schiller, P. M. Shah, M. Crawford, A. DeMaria, R. Devereux, H. Feigenbaum, H. Gutgesell, N. Reichek, D. Sahn, I. Schnittger, N. H. Silverman, and A. J. Tajik, "Recommendations for quantitation of the left ventricle by two-dimensional echocardiography. American Society of Echocardiography Committee on Standards, Subcommittee on Quantitation of Two-Dimensional Echocardiograms," *J. Am. Soc. Echocardiogr.* **2**, 358–367 (1989).

6. L. Axel and L. Dougherty, "MR imaging of motion with spatial modulation of magnetization," *Radiology* **171**, 841–845 (1989).
7. M. A. Fogel, P. M. Weinberg, A. Hubbard, and J. Haselgrove, "Diastolic biomechanics in normal infants utilizing MRI tissue tagging," *Circulation* **102**, 218–224 (2000).
8. F. J. Villarreal, L. K. Waldman, and W. Y. Lew, "Technique for measuring regional two-dimensional finite strains in canine left ventricle," *Circ. Res.* **62**, 711–721 (1988).
9. J. D'Hooge, A. Heimdal, F. Jamal, T. Kukulski, B. Bijnens, F. Rademakers, L. Hatle, P. Suetens, and G. R. Sutherland, "Regional strain and strain rate measurements by cardiac ultrasound: principles, implementation and limitations," *Eur. J. Echocardiogr.* **1**, 154–170 (2000).
10. D. Sung, R. W. Mills, J. Schettler, S. M. Narayan, J. H. Omens, and A. D. McCulloch, "Ventricular filling slows epicardial conduction and increases action potential duration in an optical mapping study of the isolated rabbit heart," *J. Cardiovasc. Electrophysiol.* **14**, 739–749 (2003).
11. N. A. Trayanova, J. Constantino, and V. Gurev, "Models of stretch-activated ventricular arrhythmias," *J. Electrocardiol.* **43**, 479–485 (2010).
12. K. C. Koch and J. vom Dahl, "Electromechanical mapping of the heart," *Curr. Opin. Cardiol.* **15**, 337–342 (2000).
13. T. Delhaas, T. Arts, F. W. Prinzen, and R. S. Reneman, "Relation between regional electrical activation time and subepicardial fiber strain in the canine left ventricle," *Pflugers Archiv.* **423**, 78–87 (1993).
14. O. P. Faris, F. J. Evans, D. B. Ennis, P. A. Helm, J. L. Taylor, A. S. Chesnick, M. A. Guttman, C. Ozturk, and E. R. McVeigh, "Novel technique for cardiac electromechanical mapping with magnetic resonance imaging tagging and an epicardial electrode sock," *Ann. Biomed. Eng.* **31**, 430–440 (2003).
15. T. Z. Evans, A. D. McCulloch, and L. K. Waldman, "Distributed activation and deformation in ventricular epicardium: effects of ventricular pacing," *15th Annual International Conference of the IEEE Engineering in Medicine and Biology Society*, San Diego, CA (1993).
16. K. Seo, M. Inagaki, S. Nishimura, I. Hidaka, M. Sugimachi, T. Hisada, and S. Sugiura, "Structural heterogeneity in the ventricular wall plays a significant role in the initiation of stretch-induced arrhythmias in perfused rabbit right ventricular tissues and whole heart preparations," *Circ. Res.* **106**, 176–184 (2010).
17. J. Huang, K. A. Cheng, D. J. Dosdall, W. M. Smith, and R. E. Ideker, "Role of maximum rate of depolarization in predicting action potential duration during ventricular fibrillation," *Am. J. Physiol. Heart Circ. Physiol.* **293**, H2530–2536 (2007).
18. A. D. Bachtel, R. A. Gray, J. B. Stohlman, E. B. Bourgeois, A. E. Pollard, and J. M. Rogers, "A novel approach to dual excitation ratiometric optical mapping of cardiac action potentials with DI-4-ANEPPS using pulsed LED excitation," *IEEE Trans. Biomed. Eng.* **58**, 2120–2126 (2011).
19. A. Savitzky and M. J. E. Golay, "Smoothing and differentiation of data by simplified least squares procedures," *Anal. Chem.* **36**, 1627–1639 (1964).
20. I. R. Efimov, D. T. Huang, J. M. Rendt, and G. Salama, "Optical mapping of repolarization and refractoriness from intact hearts," *Circulation* **90**, 1469–1480 (1994).
21. A. D. McCulloch, B. H. Smaill and P. J. Hunter, "Left ventricular epicardial deformation in isolated arrested dog heart," *Am. J. Physiol. Heart Circ. Physiol.* **252**, H233–H241 (1987).
22. M. H. Lee, S. F. Lin, T. Ohara, C. Omichi, Y. Okuyama, E. Chudin, A. Garfinkel, J. N. Weiss, H. S. Karagueuzian and P. S. Chen, "Effects of diacetyl monoxime and cytochalasin D on ventricular fibrillation in swine right ventricles,"*Am. J. Physiol. Heart Circ. Physiol.* **280**, H2689–2696 (2001).
23. C. J. Hyatt, S. F. Mironov, F. J. Vetter, C. W. Zemlin, and A. M. Pertsov, "Optical action potential upstroke morphology reveals near-surface transmural propagation direction," *Circ. Res.* **97**, 277–284 (2005).
24. R. M. Dongaonkar, R. H. Stewart, H. J. Geissler, and G. A. Laine, "Myocardial microvascular permeability, interstitial oedema, and compromised cardiac function," *Cardiovasc. Res.* **87**, 331–339 (2010).
25. C. M. Baumgarten and H. F. Clemo, "Swelling-activated chloride channels in cardiac physiology and pathophysiology," *Prog. Biophys. Mol. Biol.* **82**, 25–42 (2003).
26. A. R. Hashima, A. A. Young, A. D. McCulloch, and L. K. Waldman, "Nonhomogeneous analysis of epicardial strain distributions during acute myocardial ischemia in the dog," *J. Biomech.* **26**, 19–35 (1993).
27. N. H. Brown, H. M. Dobrovolny, D. J. Gauthier, and P. D. Wolf, "A fiber-based ratiometric optical cardiac mapping channel using a diffraction grating and split detector," *Biophys. J.* **93**, 254–263 (2007).
28. S. B. Knisley, R. K. Justice, W. Kong, and P. L. Johnson, "Ratiometry of transmembrane voltage-sensitive fluorescent dye emission in hearts," *Am. J. Physiol. Heart Circ. Physiol.* **279**, H1421–1433 (2000).
29. V. Montana, D. L. Farkas, and L. M. Loew, "Dual-wavelength ratiometric fluorescence measurements of membrane potential," *Biochem.* **28**, 4536–4539 (1989).
30. P. H. Lissberger and W. L. Wilcock, "Properties of all-dielectric interference filters. ii. filters in parallel beams of light incident obliquely and in convergent beams,"*J. Opt. Soc. Am.* **49**, 126–128 (1959).
31. R. Brandes, V. M. Figueredo, S. A. Camacho, B. M. Massie, and M. W. Weiner, "Suppression of motion artifacts in fluorescence spectroscopy of perfused hearts," *Am. J. Physiol. Heart Circ. Physiol.* **263**, H972–980 (1992).
32. M. Born, E. Wolf, and A. B. Bhatia, *Principles of Optics: Electromagnetic Theory of Propagation, Interference and Diffraction of Light*, Cambridge University Press, Cambridge, United Kingdom (2000).
33. G. K. Rohde, B. M. Dawant, and S. F. Lin, "Correction of motion artifact in cardiac optical mapping using image registration," *IEEE Trans. Biomed. Eng.* **52**, 338–341 (2005).
34. M. Svrcek, S. Rutherford, A. Y. Chen, I. Provaznik, and B. Smaill, "Characteristics of motion artifacts in cardiac optical mapping studies," *Annual International Conference of the IEEE Engineering in Medicine and Biology Society*, Minneapolis, MN (2009).
35. S. Bagwe, O. Berenfeld, D. Vaidya, G. E. Morley, and J. Jalife, "Altered right atrial excitation and propagation in connexin40 knockout mice," *Circulation* **112**, 2245–2253 (2005).
36. R. H. Keldermann, M. P. Nash, and A. V. Panfilov, "Modeling cardiac mechano-electrical feedback using reaction-diffusion-mechanics systems," *Physica D* **238**, 1000–1007 (2009).
37. J. P. Nolan, C. D. Deakin, J. Soar, B. W. Bottiger, and G. Smith, "European Resuscitation Council guidelines for resuscitation 2005, Sec. 4. Adult advanced life support," *Resuscitation* **67**, Suppl 1, S39–86 (2005).
38. M. S. Link, P. J. Wang, N. G. Pandian, S. Bharati, J. E. Udelson, M. Y. Lee, M. A. Vecchiotti, B. A. VanderBrink, G. Mirra, B. J. Maron, and N. A. Estes III, "An experimental model of sudden death due to low-energy chest-wall impact (commotio cordis)," *N. Engl. J. Med.* **338**, 1805–1811 (1998).
39. M. L. Weisfeldt and L. B. Becker, "Resuscitation after cardiac arrest," *J. Am. Med. Assoc.* **288**, 3035–3038 (2002).
40. M. R. Bristow, L. A. Saxon, J. Boehmer, S. Krueger, D. A. Kass, T. De Marco, P. Carson, L. DiCarlo, D. DeMets, B. G. White, D. W. DeVries, and A. M. Feldman, "Cardiac-resynchronization therapy with or without an implantable defibrillator in advanced chronic heart failure," *N. Engl. J. Med.* **350**, 2140–2150 (2004).